1   Supporting Information for

2   **Delineation and Fine-Scale Structure of Active Fault Zones during**

3   **the 2014-2023 unrest at the Campi Flegrei Caldera (Southern Italy)**

4   **from High-Precision Earthquake Locations**

5

6   *Francesco Scotto di Uccio*[1]*, Anthony Lomax*[2]*, Jacopo Natale*[3]*, Titouan Muzellec*[1]*, Gaetano*

7   *Festa*[1,4]*, Sahar Nazeri*[1]*, Vincenzo Convertito*[5]*, Antonella Bobbio*[5]*, Claudio Strumia*[1] *and Aldo*

8   *Zollo*[1]

9

10   [1] Department of Physics Ettore Pancini, Università di Napoli Federico II, Napoli, Italy

11   [2] ALomax Scientific, Mouans-Sartoux, France

12   [3] Department of Earth and Geoenvironmental Sciences, Università di Bari "Aldo Moro", Bari,

13   Italy

14   [4] Istituto Nazionale di Geofisica e Vulcanologia, Roma, Italy

15   [5] Osservatorio Vesuviano, Istituto Nazionale di Geofisica e Vulcanologia, Napoli, Italy

16

17   Corresponding author: Aldo Zollo (aldo.zollo@unina.it)

18

19   **Contents of this file**

20   Text from S1 to S3

21   Figure S1 to S2

22   Table S1

23

24   **Additional Supporting Information (Files uploaded separately)**

25   Captions for Movie S1 to S3

26

27   **Introduction**

28 In the Supplementary information, we present the estimation of the source parameters for the main

29 event (Md 4.2) from spectral modelling (Text S1), the details of the location technique, that has

30 been applied to the 2014-2023 Campi Flegrei arrival times and waveforms (Text S2) and the

31 estimation of the focal mechanisms for the main events (Md > 3.0) in the catalogue (Text S3).

32

33 **Text S1: Source parameters for the main event**

34 For the main event in the dataset (Md 4.2) occurred on the 2023/09/27 01:35:34 we analyzed

35 source parameters from frequency domain inversion of S-wave amplitude spectra. The inversion

36 follows the approach proposed by Supino et al. (2019), where a generalized Brune's model (Brune,

37 1970) is used to evaluate source parameters and their associated uncertainties based on integration

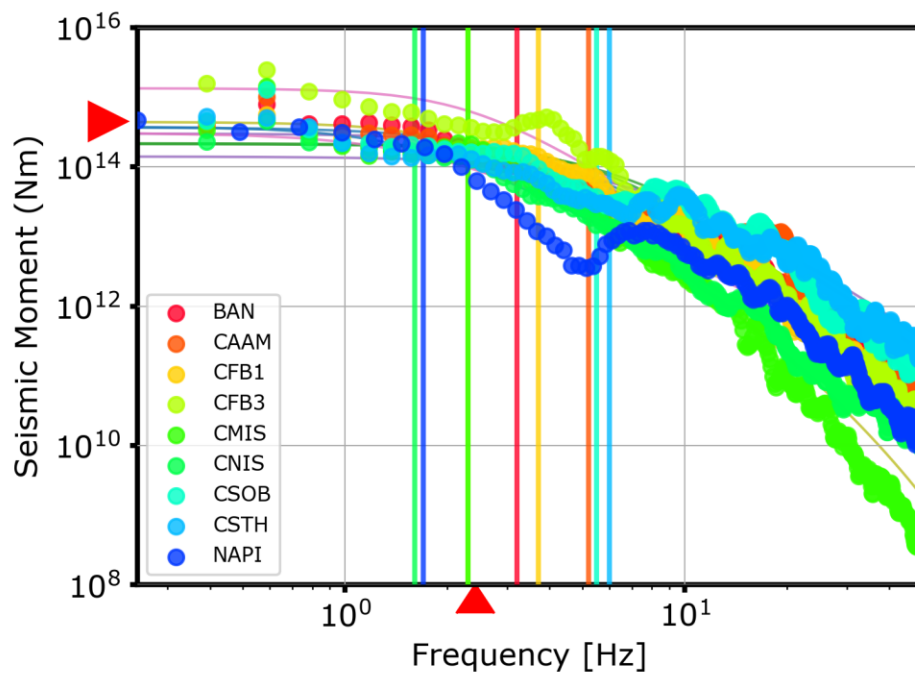38 of the a posteriori Probability Density Function (PDF) (Tarantola, 2004).

39

40

41 **Figure S1:** Spectral amplitudes (circles) and of spectral amplitudes fits (lines) with color code representing

42 the different stations. Vertical lines mark corner frequency estimations at single stations, while red arrows

43 indicate the final estimation of Seismic moment M_0 and corner frequency f_c for the event.

44

45 For the analysis the displacement amplitude spectra recorded at available nearby stations (red

46 triangles in Figure 1) were used after removal of the instrumental response. Manual picking of the

47 event allowed to select $3s$ time windows around the S wave (0.2s before and 2.8 after the pick) to

48 be used for the inversion. Anelastic attenuation was taken into account by considering a constant

49 quality factor $Q = 150$, while the wave propagation velocity was fixed to $v_s = 3000 m/s$ with

50 density $\rho = 2.5 g/cm^3$ (Judenherc and Zollo, 2004). Spectral fit is shown in Figure S1.

51 The moment magnitude was estimated to be $M_w = 3.68 \pm 0.02$ with corner frequency $f_c = 2.4 \pm$

52 $0.1\ Hz$. The stress drop from Kelis-Borok (1959) relation results $\Delta\sigma = 2.3 \pm 0.5\ MPa$. Finally,

53 the retrieved source radius $a = 460 \pm 20\ m$ suggests that the rupture process involved a fault with

54 a length of about $1 km$. The average slip was estimated to be of the order of 3-5 cm.

55

56 **Text S2: High-precision earthquake relocation procedures**

57 *General framework*

58 We obtain multi-scale high-precision earthquake relocations with NLL-SSST-coherence, which

59 combines of source-specific, station traveltime corrections (SSST) and stacking of probabilistic

60 locations for nearby event based on inter-event waveform coherence (Lomax and Savvaidis, 2022;

61 Lomax and Henry, 2023). These procedures are extensions of the NonLinLoc location algorithm

62 (Lomax et al., 2000, Lomax et al. 2014; NLL hereafter), which performs efficient, global sampling

63 to generate a posterior probability density function (PDF) in 3D space for hypocenter location.

64 This PDF provides a comprehensive description of likely hypocentral locations and their

65 uncertainty, and enables application of the waveform coherence relocation. Within NLL, we used

66 the equal differential-timing (EDT) likelihood function (Zhou, 1994; Lomax et al., 2014), which

67 is highly robust in the presence of outlier data caused by large error in phase identification,

68 measured arrival-times or predicted traveltimes. We use a finite-differences, eikonal-equation

69 algorithm (Podvin and Lecomte, 1991) to calculate gridded P and S traveltimes for initial NLL

70 locations using a smoothed version (Figure S2) of the velocity model used by the seismic

71 laboratory from INGV-Osservatorio Vesuviano (Tramelli et al., 2021).
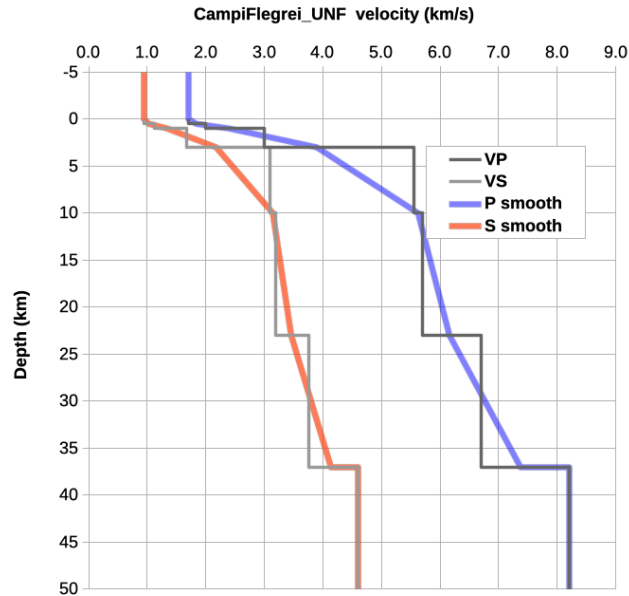
CampiFlegrei_UNF velocity (km/s)

Figure S2: Smoothed P and S velocity model, drawn from the velocity model used by the seismic laboratory at INGV-Osservatorio Vesuviano (Tramelli et al., 2021).

Source-specific station term corrections

In a first relocation stage, NLL-SSST-coherence iteratively develops SSST corrections on collapsing length scales (Richards-Dinger and Shearer, 2000; Lomax and Savvaidis, 2022), which can greatly improve, multi-scale, relative location accuracy and clustering of events. In contrast to station static corrections, which give a unique time correction for each station and phase type, SSST corrections vary smoothly throughout a 3D volume to specify a source-position dependent correction for each station and phase type. These corrections account for 3D variations in velocity structure and corresponding distortion in source-receiver ray paths. Spatial-varying, SSST corrections are most effective for improving relative locations on all scales when the ray paths between stations and events differ greatly across the studied seismicity. SSST corrections can improve multi-scale precision when epistemic error in the velocity model is large, such as when a 1D, laterally homogeneous model or a large-wavelength, smooth model is used in an area with sharp, lateral velocity contrasts or smaller scale, 3D heterogeneities.

89   *Waveform coherency relocation*

90   In a second relocation stage, NLL-SSST-coherence reduces aleatoric location error by

91   consolidating information across event locations based on waveform coherency between the events

92   (Lomax and Savvaidis, 2022). This coherency relocation, NLL-coherence, is based on the concept

93   that if the waveforms at a station for two events are very similar (e.g. have high coherency) up to

94   a given dominant frequency, then the distance separating these events is small relative to the

95   seismic wavelength at that frequency (e.g., Geller and Mueller, 1980; Poupinet et al., 1984).

96   For detailed seismicity analysis, precise, differential times between like-phases (e.g., P and S) for

97   similar events can be measured using waveform correlation methods. Differential times from a

98   sufficient number of stations for pairs of similar events allows high-precision, relative location

99   between the events, usually maintaining the initial centroid of the event positions (Waldhauser and

100   Ellsworth, 2000; Matoza et al., 2013; Trugman and Shearer, 2017).

101   NLL-coherence uses waveform similarity directly to improve relative location accuracy without

102   the need for differential time measurements or many stations with waveform data. The method

103   assumes that high coherency between waveforms for two events implies the events are nearly co-

104   located, and also that all of the information in the event locations, when corrected for true origin-

105   time shifts, should be nearly identical in the absence of noise. Then, stacking over probabilistic

106   locations for nearby events can be used to reduce the noise in this information and improve the

107   location precision for individual, target events. We measured coherency as the maximum,

108   normalized cross-correlation between waveforms from one or more stations for pairs of events

109   within a specified distance after NLL-SSST relocation (2 km in this study). We take the maximum

110   station coherence between the target event and each other event as a proxy for true inter-event

111   distances and thus as stacking weights to combine NLL-SSST location probability density

112   functions (PDF's) over the events. In effect, this stack directly improves the hypocenter location

113   for each target event by combining and completing arrival-time data over nearby events and

114   reducing aleatoric error in this data such as noise, outliers and missing arrivals.

115   See Lomax and Savvaidis (2022) and Lomax and Henry (2023) for more discussion and details,

116   while NLL-SSST-coherence processing parameters used in this study are available on Zenodo at

117   the link https://doi.org/10.5281/zenodo.10260849 (Lomax, 2023).

118

119

120

Text S3: Focal mechanism determination

To determine in detail the fault geometry highlighted by the larger magnitude events from the mid of August until the beginning of October 2023, we computed the focal mechanisms with the code FPFIT (Reasenberg, 1985) for 7 onshore events with duration magnitude larger than 3.6, and the two larger magnitude events occurring offshore (See Figure 4). We estimated the polarity of the first P-arrival as measured on velocity sensors of the INGV network by considering only stations at a maximum epicentral distance of 8 km. An average of 11 P-polarities are available for each of the analyzed events. We used the locations, for computing azimuth and take-off angles as the ones obtained by the SSST-waveform coherence method assuming the same 1D velocity model used for earthquake locations. The best fault-plane strike, dip and rake angles for each event can be found in Table S1 together with the plot of the polarities on the focal sphere in Figure S3.

132

Event	Date	Time	Lat (°)	Long (°)	Depth (km)	Md	Strike F1/F2 (°)	Dip F1/F2 (°)	Rake F1/F2 (°)	Nb polarity
1	18/08/2023	04:09:59.42	40.8292	14.1487	2.4	3.2	30 / 210 ± 10	75 / 15 ± 3	-90 / -90 ± 5	14
2	18/08/2023	04:18:05.68	40.8300	14.1395	2.4	3.6	35 / 270 ± 0	68 / 35 ± 15	-118 / -40 ± 20	13
3	18/08/2023	04:22:49.91	40.8280	14.1388	2.1	3.1	95 / 318 ± 3	25 / 71 ± 8	-130 / -73 ± 15	13
4	07/09/2023	17:45:28.84	40.8295	14.1480	2.5	3.8	75 / 255 ± 3	60 / 30 ± 5	-90 / -90 ± 5	12
5	22/09/2023	09:02:00.02	40.8285	14.1415	1.8	3.0	48 / 270 ± 5	75 / 20 ± 13	-103 / -50 ± 15	13
6	26/09/2023	07:10:29.59	40.8063	14.1117	3.4	3.3	270 / 180 ± 3	60 / 90 ± 15	-180 / -30 ± 10	10
7	27/09/2023	01:35:34.39	40.8173	14.1553	2.9	4.2	30 / 274 ± 23	80 / 22 ± 8	-110 / -27 ± 25	8
8	02/10/2023	20:08:26.74	40.8297	14.1482	2.5	4.0	232 / 350 ± 10	78 / 25 ± 8	-68 / -150 ± 5	12
9	16/10/2023	10:36:21.14	40.8253	14.1420	1.8	3.6	18 / 220 ± 13	67 / 25 ± 5	-99 / -70 ± 40	9

133

Table S1: Location information of the larger magnitude events and description of the two planes in terms of strike, dip and rake from focal mechanisms together with the uncertainties. Events are numbered according to figure 4. Number of used polarities are reported for each event.
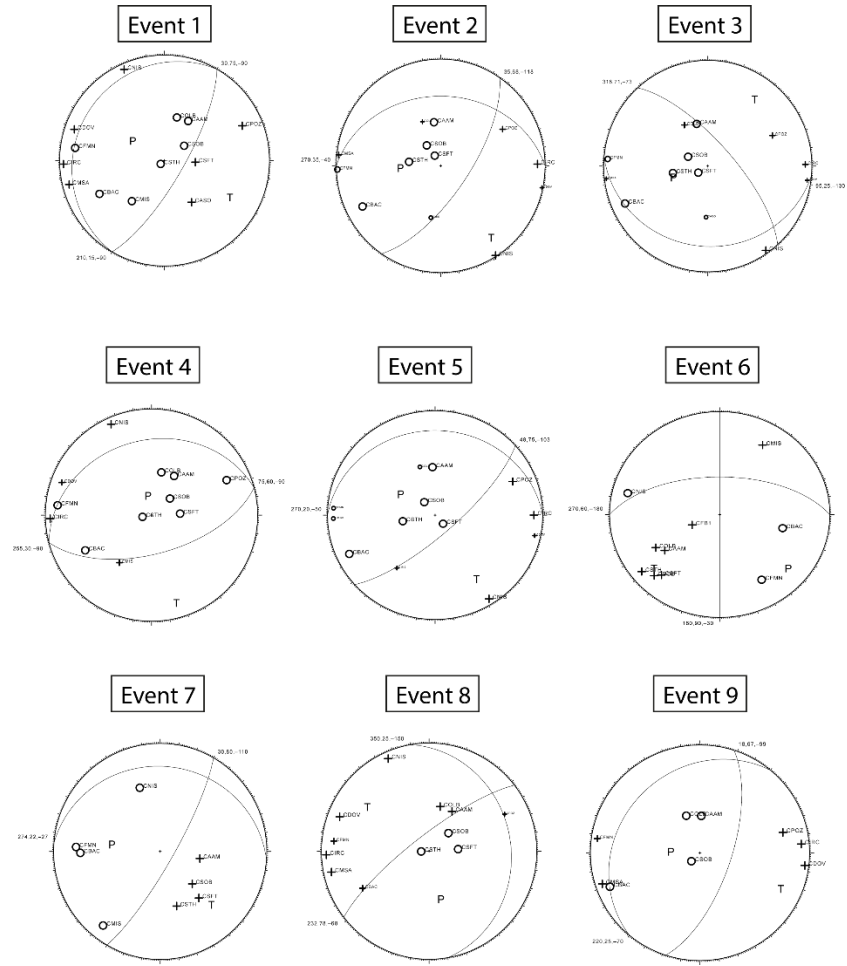
Figure S3: Focal mechanism solutions of the larger magnitude events with the polarity measurements projected on the focal sphere. Events are numbered according to figure 4.

Caption for Movie S1.

The video provides a 3D view of the 2014-2023 seismicity at the Campi Flegrei caldera, rotating the view along a E-W oriented horizontal axis.

Caption for Movie S2.

The video provides a 3D view of the 2014-2023 seismicity at the Campi Flegrei caldera, rotating the view along the azimuth.

Caption for Movie S3.

The video provides a 2D view of the yearly seismicity at the Campi Flegrei caldera, using the same representation of Figure 2.